

The Effects of Zinc Oxide (ZnO) Quantum Dots (QDs) Embedment on the Physicochemical Properties and Photocatalytic Activity of Titanium Dioxide (TiO₂) Nanoparticles

Anwar Iqbal,^{1*} Usman Saidu,¹ Farook Adam,¹ Srimala Sreekantan,²
Normawati Jasni,¹ and Mohammad Norazmi Ahmad³

¹School of Chemical Sciences, Universiti Sains Malaysia, 11800 Pulau Pinang, Malaysia

²School of Materials and Mineral Resources Engineering, Universiti Sains Malaysia,
Engineering Campus, 14300 Nibong Tebal, Seberang Perai Selatan,
Pulau Pinang, Malaysia

³Experimental and Theoretical Research Lab, Department of Chemistry, Kulliyah of
Science, International Islamic University Malaysia, 25200 Kuantan, Pahang, Malaysia

*Corresponding author: anwariqbal@usm.my

Published online: 25 August 2021

To cite this article: Iqbal, A. et al. (2021). The effects of zinc oxide (ZnO) quantum dots (QDs) embedment on the physicochemical properties and photocatalytic activity of titanium dioxide (TiO₂) nanoparticles. *J. Phys. Sci.*, 32(2), 71–85. <https://doi.org/10.21315/jps2021.32.2.6>

To link to this article: <https://doi.org/10.21315/jps2021.32.2.6>

ABSTRACT: *In this study, a detailed investigation on the effect of zinc oxide (ZnO) quantum dots (QDs) embedment on the physicochemical properties of anatase titanium dioxide (TiO₂) was conducted. The highly porous nanocomposite labelled as ZQT was prepared via the sol-gel assisted hydrothermal method. The powder X-ray diffraction (XRD) analysis indicates that the average crystallite size of the ZnO QDs, anatase TiO₂ (TiO₂NPs) and ZQT were 4.45 nm, 9.22 nm and 11.38 nm, respectively. Photoluminescent (PL) analysis detected the presence of defects related to TiO₂, oxygen vacancies and quantum confinement effect (QCE) of the ZnO QDs in ZQT. These features enhanced the photodegradation of tetracycline (TC) under 48 watt of fluorescent light irradiation when ZQT (98.0%) was used compared to TiO₂NPs (32.4%) and ZnO QDs (68.8%). The photodegradation activity was driven by O₂^{•-} followed by •OH and h⁺.*

Keywords: ZnO, TiO₂, quantum dots, photocatalysis, tetracycline

1. INTRODUCTION

Many research interests focused on the advanced oxidation processes (AOPs) to eliminate antibiotics pollutants since they are effective compared to traditional wastewater treatment techniques.¹ The AOPs are the techniques involving the generation of highly reactive hydroxyl radical ($\cdot\text{OH}$) to destroy a wide range of organic pollutants.² Among various AOPs, heterogeneous photocatalysis is regarded as the most efficient technique for degrading organic contaminants into innocuous compounds.²

Semiconductors incorporated with quantum dots (QDs) are a new class of photocatalysts that have drawn extensive interest for their quantum confinement effect (QCE), high extension coefficient and larger surface-to-volume ratio. The QCE leads to the bandgap widening, resulting in the generation of energetic photoelectrons required for oxygen reduction.³ The QDs/semiconductor nanocomposite have been developed using various methods.⁴⁻⁷ However, most of these methods required an ageing time of more than 24 h and higher temperatures (200°C to 400°C). It is also difficult to control the coverage and the sizes of the QDs.⁸

In this work, a zinc oxide (ZnO) QDs/titanium dioxide (TiO₂) nanocomposite was synthesised using a sol-gel assisted hydrothermal method. The sol-gel method allows the nanocomposite to be prepared at a mild temperature and allows better control of the QDs size and coverage. The obtained nanocomposite showed higher efficiency than the pristine TiO₂ and ZnO QDs in the photodegradation of tetracycline (TC) antibiotic.

2. EXPERIMENTAL

2.1 Synthesis of Zinc Oxide Quantum Dots (ZnO QDs)

The synthesis of ZnO QDs was carried out according to the method reported by Mahjoub et al. with some modifications.⁹ A 50.0 ml solution of zinc acetate (0.1M) was prepared by dissolving 4.4 g of zinc acetate dihydrate (Sigma Aldrich, $\geq 98\%$, Selangor, Malaysia) in 200 ml of methanol (QReC) under vigorous stirring. The zinc acetate solution pH was reduced to pH 14 by adding KOH (QReC) (1 M) solution drop by drop to obtain the ZnO QDs. The mixture was stirred for 1 h using a magnetic stirrer. To control the particle size, tetraethylorthosilicate (TEOS, Acros Organics, 98%, Fair Lawn, NJ) solution (0.25 ml) was added, followed by distilled water (0.5 ml) to initiate the sol-gel

reaction of silica on the surface of the ZnO QDs. The ZnO QDs was obtained by centrifugation and washed three times with methanol and distilled water to remove unreacted reactants. The obtained ZnO QDs was dried in the oven at 100°C for 12 h.

2.2 Synthesis of ZnO QDs/TiO₂ Nanocomposite

Titanium(IV) tetraisopropoxide (TTIP, Across Organic, > 98%, Fair Lawn, NJ), solution (5.90 ml) was added into 200 ml of an aqueous solution containing 2.0 g of soluble starch (Fisher Scientific, Leicestershire, UK). The solution was stirred for 10 min at 65°C. The solution's pH was adjusted to pH 9 by adding the ammonium hydroxide solution dropwise. The ZnO QDs (0.81 g) was added to the TiO₂ sol and stirred for another 1 h at 85°C. Finally, the mixture was centrifuged, and the obtained product was washed four times with ethanol (QReC chemical, > 99.7%) and distilled water. It was then dried at 100°C for 12 h and calcined at 500°C for 2 h with a heating rate of 3°C min⁻¹. The obtained ZnO QDs/TiO₂ nanocomposite was labelled as ZQT. For comparison, pristine TiO₂ NPs was synthesised similarly but without ZnO QDs.

2.3 Characterisation ZnO QDs/TiO₂ Nanocomposite

The crystalline phase and crystallite size of the synthesised samples were investigated using powder X-ray diffraction (XRD) techniques. The XRD patterns were recorded on a BRUKER AXS D8, Germany advanced X-ray diffractometer with Cu-K α radiation ($\lambda = 0.15478$ nm). The 2θ range was set between 20° to 80°. The field emission scanning electron microscope and energy dispersive X-ray (FESEM/EDX) analysis was used to determine the morphology and the elemental composition of the samples, employing Leo Supra 50Vp FESEM, Netherland. High-resolution transmission electron microscopy (HRTEM) was used for the texture analysis, employing HRTEM 200 kV with Field Emission, TECNAI G2 20 S-TWIN, FEI, resolution below 100 nm, USA). The nitrogen adsorption-desorption (NAD) analysis (Micromeritic ASAP 2020 Surface Adsorption Porosimeter [SAP], USA) was used to estimate the surface area and the porosity of the synthesized samples. The nanocomposites optical properties were measured using the solid-state UV/Vis diffuse reflectance spectroscopy (PerkinElmer Lambda 35 UV/VIS Spectrometer, USA) method by scanning the reflectance of the samples in the range of 200 nm to 800 nm. Photoluminescence (PL) spectra were measured at room temperature using PerkinElmer LS 55, USA fluorescence spectrophotometer at an excitation wavelength of 325 nm.

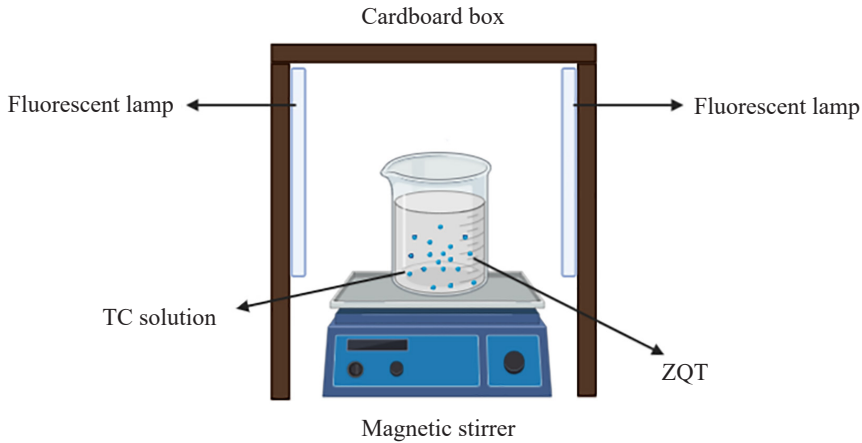


Figure 1: Homemade reactor used in the photodegradation of tetracycline.

2.4 Photocatalytic Activity

The photocatalytic performance of the nanocomposite was investigated by monitoring the photodegradation of TC in an aqueous solution using a homemade reactor (Figure 1) equipped with two fluorescent lights (48 W). The light intensity was determined to be 104.4 W/m², whereas the residual UV leakage of the visible light was detected to be 0.40 W/m². The measurement was carried out using Dual-Input Data Logging Radiometer (Model PMA2100, Pennsylvania, USA) equipped with visible, UVA + UVB detectors. In each experiment, 50 mg of the photocatalyst was dispersed in 200 ml of TC solution (20 mg l⁻¹). Before the light irradiation, the suspension was magnetically stirred in the dark for 30 min to reach adsorption-desorption equilibrium. An aliquot from the suspension was then collected at regular time intervals and filtered using a 0.22 μm membrane filter. The change in TC concentration was determined using a UV-vis spectrophotometer (UV2600, Shimadzu, Japan). The degradation percentage of the TC was calculated using the following equation:

$$R (\%) = 1 - \frac{C_t}{C_0} \quad (1)$$

Where C_0 represent the concentration before light irradiation, C_t is the concentration at a determined reaction time, and R is the percentage of TC photodegradation. The determination of the residual TC concentration was determined using the maximum absorbance at 358 nm.

3. RESULTS AND DISCUSSION

3.1 XRD Analysis

The XRD patterns of the materials are presented in Figure 2(a). The diffractogram of TiO₂ NPs shows the diffraction peaks of 2θ at 25.3°, 37.8°, 48.1°, 54.1°, 55.1°, 62.7°, 68.7°, 70.3° and 75.2° equivalent to the (101), (004), (200), (105), (211), (204), (116), (220), (215) and (224) planes.

These planes refer to the tetragonal structure of the anatase TiO₂ phase (JCPDS 00-021-1272). The narrow and pointed diffraction peaks confirmed the high crystallinity of the anatase TiO₂ phase.¹⁰

The XRD patterns of the as-synthesised ZnO QDs show broad diffraction peaks at 2θ values of 31.8°, 34.5°, 36.3°, 47.6°, 56.6°, 63.0° and 66.4° corresponding to the crystal planes (100), (002), (101), (102), (110), (103) and (200) of hexagonal wurtzite phase of ZnO (JCPDS 36-1451). As can be seen from the XRD patterns of ZQT, the crystalline planes indexed to the anatase TiO₂ broadened when the ZnO QDs was incorporated into the crystal lattice of the anatase TiO₂. The broadness of the XRD peaks indicates the formation of smaller size ZnO QDs crystallites.¹¹ The average crystallite sizes as measured using the Debye–Scherrer equation (Equation 2) are 11.38 nm, 4.45 nm, and 9.22 nm for the TiO₂ NPs, ZnO QDs and ZQT, respectively.

$$D = \frac{k\lambda}{\beta \cos \theta} \quad (2)$$

Where D is the crystallite size, λ is the wavelength equal to 0.154 nm, k is a constant taken as 0.94, β is the full widths at half-maximum intensity (FWHM), and θ is the Bragg angle of the actual peak.

Diffraction peaks related to ZnO QDs were not observed in the diffractogram of ZQT. As the crystal framework of anatase was being built, it will induce strains to the crystal framework of the ZnO QDs. The strains may have caused the ZnO QDs to lose their crystallinity.¹² As a result, crystalline peaks related to ZnO QDs were not detected. A lower concentration of ZnO QDs can also cause the absence of diffraction peaks.¹³

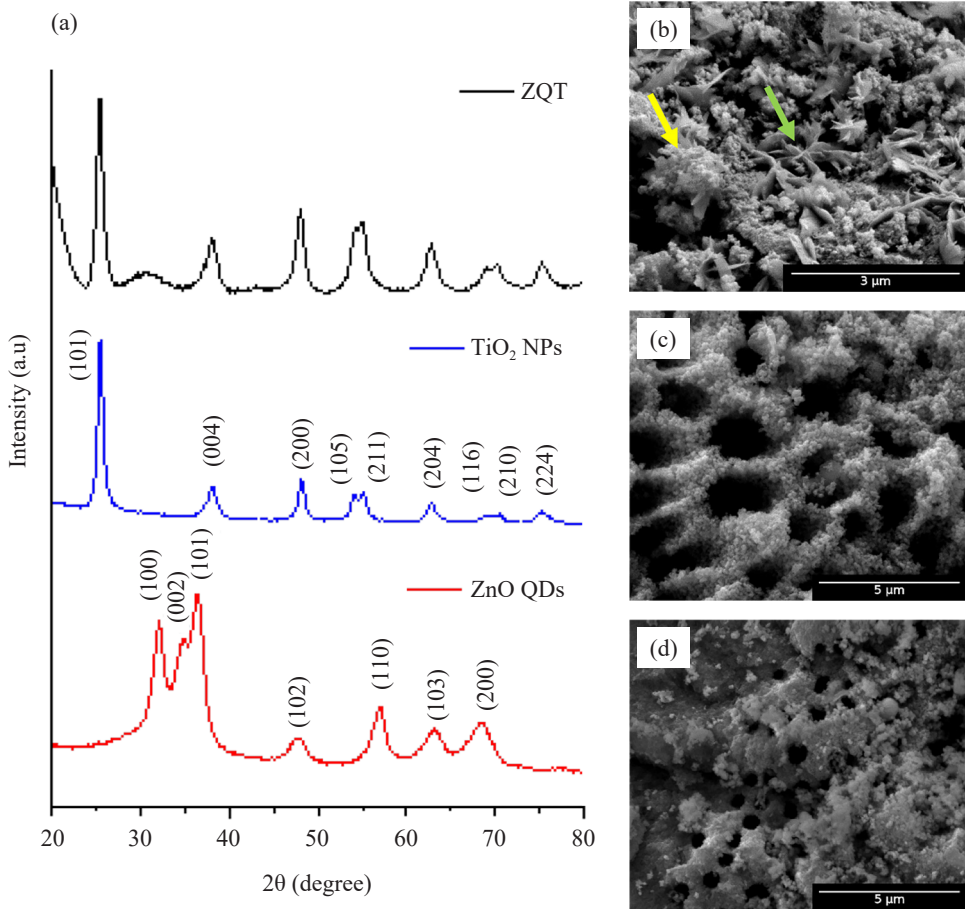


Figure 2: (a) XRD patterns of ZQT, TiO₂ NPs, and ZnO QDs, SEM images of (b) ZnO QDs, (c) TiO₂ NPs, and (d) ZQT.

3.2 Morphology Study

The FESEM images of ZnO QDs are shown in Figure 2(b). The ZnO QDs was observed to contain irregularly spherical shaped particles (shown using a yellow arrow) and nanoflakes (shown using a green arrow). The formation of nanoflakes could be due to the rapid deposition of the ZnO QDs on top of the spherically shaped particles and begin growing upwards. The ZnO QDs can be attracted to each other due to electrostatic attraction.

Starch was added as a template to create pores on the surface of the anatase TiO_2 . In hot water, the starch molecules will swell as a result of weakened hydrogen bonds. Due to the presence of Van der Waals forces, the TiO_2 sols will be driven to be adsorbed around the starch molecules. The starch granules removed during the calcination process, leaving behind pores, as shown in Figure 2(c).¹⁴ The average pore diameter was measured to be $1.67 \mu\text{m}$. The added ZnO QDs and TiO_2 NPs reacted to form a new composite layer and with an average pore diameter of $0.51 \mu\text{m}$ (Figure 2[d]).

3.3 Optical Absorption Property

The UV-vis absorption spectra of TiO_2 NPs and ZQT are presented in Figure 3(a). The ZnO QDs was observed to have the lowest optical edge due to the quantum confinement effect (QCE). As the size of the increases, the optical band edge shifted to a higher wavelength. All the nanocomposites indicate good absorptivity in the UV region. The bandgap energies of the synthesised samples were calculated using Tauc's equation as follows:

$$\alpha h\nu = A (h\nu - E_g)^{n/2} \quad (3)$$

Where α is the absorption coefficient, h is Planck's constant, ν is the light frequency, A is the proportionality constant, and E_g is the bandgap energy. The value of n depends on the type of optical transition in the semiconductor, whether direct ($n = 1$) or indirect ($n = 4$) transition. The bandgap energies of the nanocomposites were estimated from the plot of $(\alpha h\nu)^{1/2}$ versus $h\nu$ as shown in the inset of Figure 3(a). The values were found to be 3.10 eV, 3.50 eV and 3.42 eV for TiO_2 NPs, ZnO QDs and ZQT, respectively. The Mulliken electronegativity theory was used to calculate the potentials of the valence band (VB) and the conduction band (CB) edges:

$$E_{VB} = X - E^e + 0.5E_g \quad (4)$$

$$E_{CB} = E_{VB} - E_g \quad (5)$$

The E_{VB} is the valence band edge potential, E_{CB} is the conduction band potential, E_g is the bandgap of the semiconductor, E^e is the energy of free electrons on the hydrogen scale (~ 4.5 eV), and X is the electronegativity of the semiconductor, which is 5.79 eV and 5.81 eV for ZnO QDs and TiO_2 NPs, respectively.¹⁵ The CB and VB potentials calculated using Equations 4 and 5 are given in Table 1.

The calculated VB potential was 2.87 eV for ZnO QDs, 2.95 eV for TiO₂ NPs, and 2.93 eV for ZQT. The values are higher than the standard redox potentials of the oxidising agents such as $\bullet\text{OH}/\text{HO}^-$ (1.99 eV), H_2O_2 (1.77 eV), and O_3 (2.07 eV), suggesting that the synthesised nanocomposite may have stronger oxidation abilities.¹⁶ The calculated CB potential for the TiO₂ NPs was more positive compared to ZnO QDs due to the QCE. The QCE shifts the CB to more negative potentials (on the NHE scale) with decreasing particle size, leading to the generation of species with higher oxidation ability.

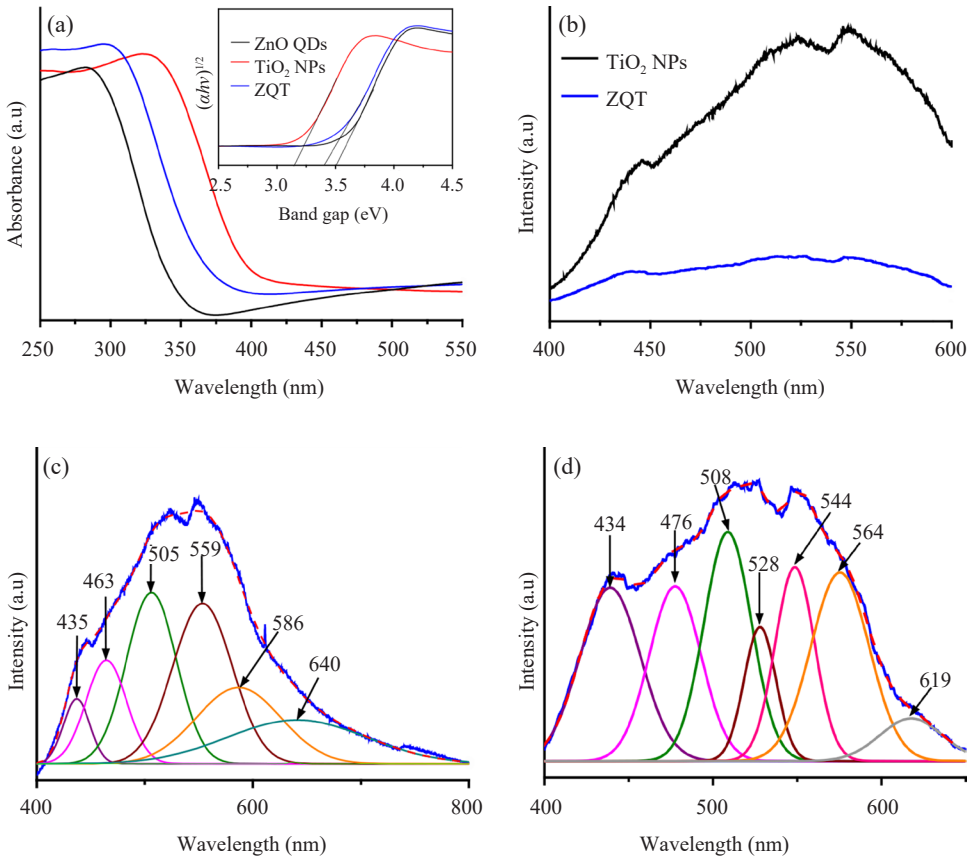


Figure 3: (a) UV-vis diffuse reflectance spectra with estimated energy gap (inset), (b) photoluminescence (PL) spectra of TiO₂ NPs and ZQT, (c) deconvoluted PL spectrum of TiO₂ NPs, and (d) deconvoluted PL spectrum of ZQT.

Table 1: The VB and CB potentials of the ZnO QDs, m-TiO₂ and ZQT.

Samples	Band gap E_g (eV)	VB edge (eV)	CB edge (eV)
ZnO QDs	3.50	2.87	-0.46
TiO ₂ NPs	3.10	2.95	-0.15
ZQT	3.24	2.93	-0.30

3.4 Photoluminescence Study

The PL intensity of ZQT was observed to be lower compared to TiO₂ NPs (Figure 3[b]), indicating that the separation of photogenerated e^-/h^+ pairs in ZQT is better than TiO₂ NPs.¹⁷ Four Gaussian bands were formed when the broad band of TiO₂ NPs was deconvoluted (Figure 3[c]). The first Gaussian band at 435 nm is attributed to the self-trapped excitons of TiO₆ octahedra.¹⁸ The Gaussian band at 463 nm indicate the shallow trap due to the Ti³⁺ states just below the conduction band, whereas the band at 505 nm is due to the deep trap state associated with the single electron trapped oxygen vacancy.¹⁹ The transitions of electrons from the conduction band edge to deep trap holes related to oxygen vacancies is indicated by the presence of a Gaussian band at 559 nm.¹⁹ The intrinsic defects in the TiO₂ NPs framework may have given rise to the Gaussian band at 586 nm. The Gaussian band at 640 nm is associated with the surface oxygen of hydroxyl species which can create an acceptor level above the VB of the TiO₂ NPs.²⁰

The ZQT's PL spectrum deconvolution resulted in six Gaussian bands indicating the formation of new defects sites (Figure 3[d]). The strong QCE of the ZnO QDs is indicated by a Gaussian band at 434 nm.²¹ The Gaussian band at 476 nm is attributed to the shallow trap assigned to the Ti³⁺ states just below the conduction band.¹⁹ The Gaussian band at 508 nm is due to the non-radiative electron capture from the CB by a singly charged oxygen (V_o^+) vacancy leading to an unstable state that recombines with photogenerated holes in the VB .²² The transition of electrons from CB to an oxygen antisite, O_{zn} is shown by the Gaussian band at 528 nm.²³ The Gaussian band at 544 nm is proposed to be due to the $CB \rightarrow O_i$ transition by.^{24,25} The deeply trapped double-charged oxygen (V_o^{++}) vacancy state, which undergoes recombination with a CB electron, gives rise to the Gaussian band at 564 nm and 619 nm.¹⁷

3.5 Photooxidation of Tetracycline

The photocatalytic potential of the ZQT was tested in the photooxidation of tetracycline (TC) in an aqueous solution under fluorescent light irradiation. The photooxidation profiles are presented in Figure 4(a). Without ZQT, TC was not

degraded, indicating TC's sufficient stability and the negligible self-photolysis effect. Both TiO₂ NPs and ZnO QDs were able to photooxidise 32.4% and 68.8% of TC, respectively. The photooxidation of TC significantly enhanced up to 98.0% when ZQT was used. The higher photocatalytic activity of ZQT is attributed to the QCE of the ZnO QDs, besides the presence of various types of defects related to TiO₂ NPs. The QCE will produce photogenerated e^-/h^+ pairs that are highly energetic and capable of photooxidising pollutants. The TC photooxidation rate constant, k was obtained based on the apparent first-order rate equation (Equation 6). The results are presented in Figure 4(b).

$$-\ln(C/C_0) = kt \quad (6)$$

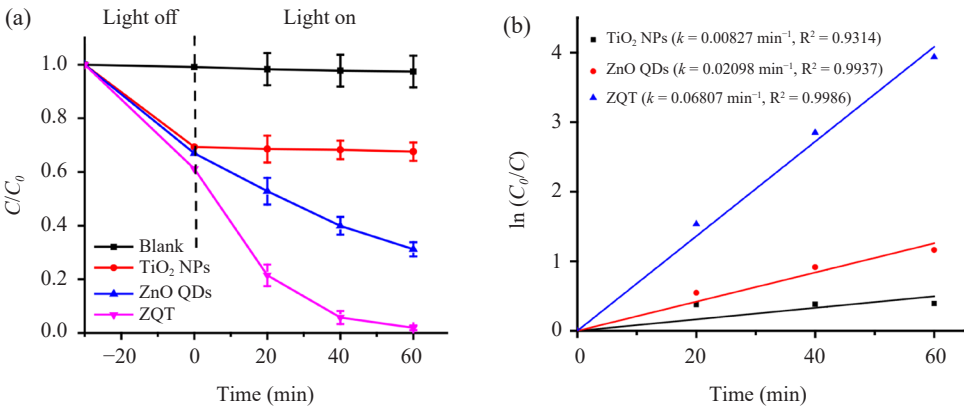


Figure 4: (a) Photocatalytic degradation of TC using different catalysts, and (b) kinetic curve to evaluating the rate constants (k).

Scavenging tests were conducted to identify the active species responsible for the photodegradation of TC. Ascorbic acid (AA), triethanolamine (TEA), and isopropanol (IPA) were used as a scavenging agent for $O_2^{\bullet-}$, h^+ , and $\bullet OH$, respectively.^{26–29} From the TC removal profile shown in Figure 5(a), the TC removal dropped to 21.87% and 60.94% when AA and IPA were added, whereas, in the presence of TEA, 73.27% of TC was removed, respectively. Hence, the major species involved in the photodegradation process was $O_2^{\bullet-}$ followed by $\bullet OH$ and h^+ . Based on the scavenging test data, the flow of photogenerated e^-/h^+ is proposed. From Table 1, the TiO₂ NPs has the CB and VB potential of 2.95 eV and -0.15 eV, respectively. The CB and VB potential of ZnO QDs is 2.87 eV and -0.46 eV, respectively. When irradiated, electrons from the VB band of both semiconductors will be excited to their respective CB . Since the reduction potential of oxygen ($E^0(O_2/O_2^{\bullet-}) = -0.33$ eV/NHE) is more negative than the CB potential of TiO₂ NPs, it will not have enough reduction abilities to

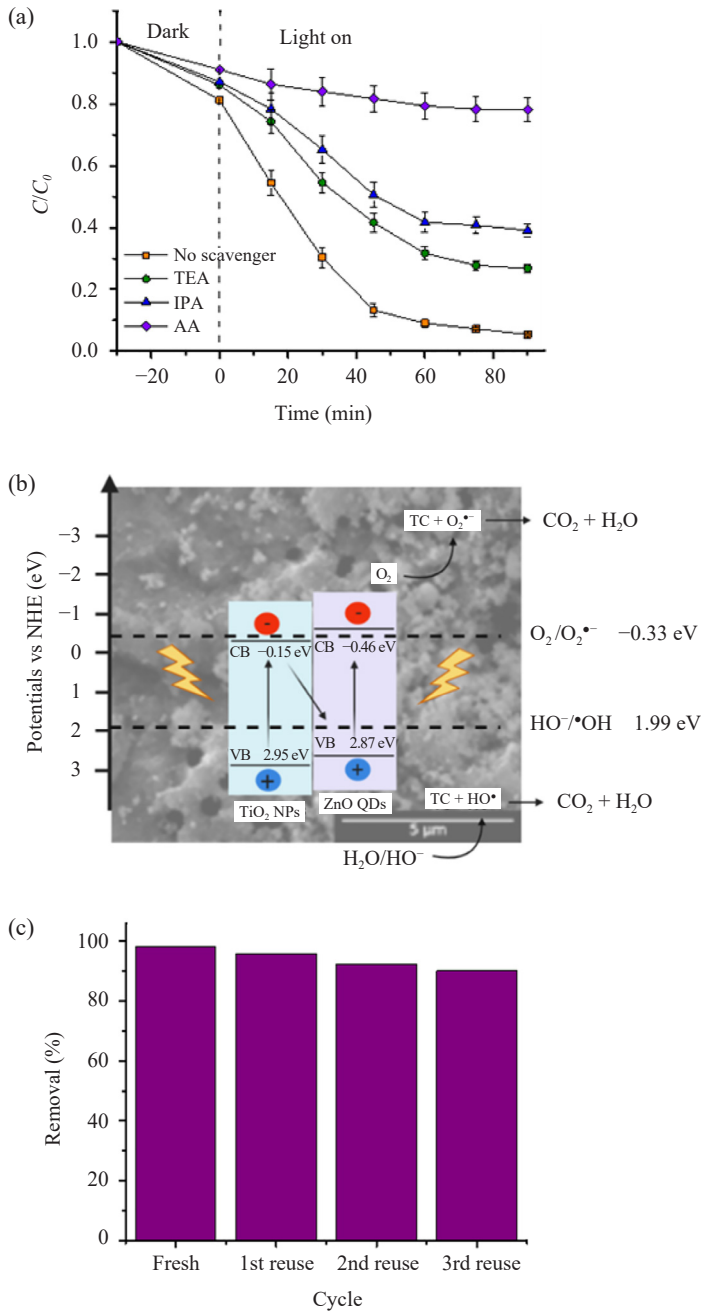


Figure 5: (a) Photocatalytic degradation of TC in the presence of different scavengers, (b) the flow of photogenerated electron/hole pairs, and (c) the reusability profile.

generate O₂^{•-} species from dissolved O₂. Hence, the Z-scheme heterojunction is proposed since the *CB* potential of ZnO QDs can generate O₂^{•-} species. The potential of the photogenerated holes in the *VB* of TiO₂ NPs is positive enough to oxidise OH⁻ to •OH (E⁰ (OH⁻/•OH) = +1.99 eV) and H₂O to •OH (E⁰ (H₂O/•OH) = +2.34 eV). The photogenerated electrons in the *CB* of TiO₂ NPs will migrate to the *VB* band of ZnO QDs to recombine with the photogenerated holes. Based on the Z-scheme, the photogenerated electrons will accumulate in the *VB* of ZnO QDs, whereas the holes will remain in the *CB* band of the TiO₂ NPs. Hence, the pairs can be separated effectively. The generated O₂^{•-} and •OH radicals can effectively degrade the TC into CO₂ and H₂O. The flow of photogenerated e⁻/h⁺ pairs, according to the Z-scheme, is shown in Figure 5(b). Figure 5(c) shows the reusability profile of ZQT in TC photodegradation. The ZQT experienced ~8% loss in its photocatalytic activity at the end of four cycles. The small degree of loss indicates that ZQT has good stability.

4. CONCLUSION

In this study, a highly porous ZQT nanocomposite was successfully prepared by embedding ZnO QDs within the matrix of anatase TiO₂ through sol-gel assisted hydrothermal method. The embedment of ZnO QDs introduced its quantum confinement effect (QCE) to the anatase TiO₂. The QCE and the defects related to TiO₂ and oxygen vacancies significantly enhanced the photodegradation of tetracycline (TC) compared to TiO₂ NPs. The QCE will produce photogenerated electron/hole pairs with higher energy. At the same time, the presence of Z-scheme heterojunction suppressed the recombination rate of the photogenerated e⁻/h⁺ pairs. In ZQT's presence, 98% of TC was removed, whereas 32.4% and 68.8% of TC was removed when TiO₂ NPs and ZnO QDs were used.

5. ACKNOWLEDGEMENTS

This research was supported by Universiti Sains Malaysia Research University Grant (RUI) (1001/PKIMIA/8011083). Usman Saidu acknowledges Sule Lamido University Kafin Hausa, Nigeria, for the PhD sponsorship awarded to him through Tertiary Education Trust Fund (TETFund).

6. REFERENCES

1. Ahmed, S. N. & Haider, W. (2018). Heterogeneous photocatalysis and its potential applications in water and wastewater treatment: A review. *Nanotechnology*, 29(34), 342001. <https://doi.org/10.1088/1361-6528/aac6ea>
2. Li, D. & Shi, W. (2016). Recent developments in visible light photocatalytic degradation of antibiotics. *Chinese J. Catal.*, 37(6), 792–799. [https://doi.org/10.1016/s1872-2067\(15\)61054-3](https://doi.org/10.1016/s1872-2067(15)61054-3)
3. Yang, J. et al. (2018). BiVO₄ quantum tubes loaded on reduced graphene oxide aerogel as efficient photocatalyst for gaseous formaldehyde degradation. *Carbon*, 138, 118–124. <https://doi.org/10.1016/j.carbon.2018.06.003>
4. Miodyńska, M. et al. (2020). Urchin like TiO₂ structures decorated with lanthanide doped Bi₂S₃ quantum dots to boost hydrogen photogeneration performance. *Appl. Catal. B.*, 272, 118962. <https://doi.org/10.1016/j.apcatb.2020.118962>
5. Zhang, D. et al. (2019). The in situ ligand exchange linker assisted assembly of oil soluble CdSe quantum dots to TiO₂ films. *Appl. Surf. Sci.*, 475, 813–819. <https://doi.org/10.1016/j.apsusc.2018.12.289>
6. Chen, S., Li, C. & Hou, Z. (2019). A novel in situ synthesis of TiO₂/CdS heterojunction for improving photoelectrochemical water splitting. *Int. J. Hydrog. Energ.*, 44(47), 25473–25485. <https://doi.org/10.1016/j.ijhydene.2019.08.049>
7. Basheva, E. S. et al. (2020). In situ growth of CdS quantum dots on phosphorus doped carbon nitride hollow tubes as active 0D/1D heterostructures for photocatalytic hydrogen evolution. *J. Colloid Interface Sci.*, 577, 1–11. <https://doi.org/10.1016/j.jcis.2020.05.053>
8. Ghows, N. & Entezari, M. H. (2012). Sono synthesis of core shell nanocrystal (CdS/TiO₂) without surfactant. *Ultraso. Sonochem.*, 19(5), 1070–1078. <https://doi.org/10.1016/j.ultsonch.2012.01.009>
9. Mahjoub, M. A. et al. (2016). Synthesis and study of stable and size controlled ZnO SiO₂ quantum dots: Application as a humidity sensor. *J. Phys. Chem. C.*, 120(21), 11652–11662. <https://doi.org/10.1021/acs.jpcc.6b00135>
10. Yin, Q. et al. (2016). Preparation of highly crystalline mesoporous TiO₂ by sol-gel method combined with two-step calcining process. *J. Expl. Nanosci.*, 11(14), 1127–1137. <https://doi.org/10.1080/17458080.2016.1189097>
11. Qiao, B. et al. (2016). Synthesis of ZnO quantum dots and their agglomeration mechanisms along with emission spectra based on ageing time and temperature. *Chin. Phys. B.*, 25(9), 098102. <https://doi.org/10.1088/1674-1056/25/9/098102>
12. Iqbal, A. et al. (2021). Floating ZnO QDs-modified TiO₂/LLDPE hybrid polymer film for the effective photodegradation of tetracycline under fluorescent light irradiation: Synthesis and characterisation. *Molecules*, 26, 2509. <https://doi.org/10.3390/molecules26092509>

13. Chen, Q. et al. (2018). Ultrafine ZnO quantum dot modified TiO₂ composite photocatalysts: The role of the quantum size effect in heterojunction enhanced photocatalytic hydrogen evolution. *Catal. Sci. Technol.*, 8(5), 1296–1303. <https://doi.org/10.1039/c7cy02310c>
14. Muniandy, S. S. et al. (2017). Green synthesis of mesoporous anatase TiO₂ nanoparticles and their photocatalytic activities. *RSC Adv.*, 7(76), 48083–48094. <https://doi.org/10.1039/C7RA08187A>
15. Jiang, Y. et al. (2018). Facile in-situ solvothermal method to synthesise double shell ZnIn₂S₄ nanosheets/TiO₂ hollow nanosphere with enhanced photocatalytic activities. *Ceram. Int.*, 44(6), 6115–6126. <https://doi.org/10.1016/j.ceramint.2017.12.244>
16. Li, W. et al. (2018). Photocatalytic degradation of tetracycline hydrochloride via a CdS-TiO₂ heterostructure composite under visible light irradiation. *Nanomaterials*, 8(6), 415. <https://doi.org/10.3390/nano8060415>
17. Imam, S. S., Adnan, R. & Kaus, N. H. M. (2018). Influence of yttrium doping on the photocatalytic activity of bismuth oxybromide for ciprofloxacin degradation using indoor fluorescent light illumination. *Res. Chem. Intermed.*, 44(9), 5357–5376. <https://doi.org/10.1007/s11164-018-3427-8>
18. Paul, K. K. & Giri, P. K. (2017). Role of surface plasmons and hot electrons on the multi step photocatalytic decay by defect enriched Ag@TiO₂ nanorods under visible light. *J. Chem. C.*, 121(36), 20016–20030. <https://doi.org/10.1021/acs.jpcc.7b05328>
19. Khan, H. & Swati, I. K. (2016). Fe³⁺-doped anatase TiO₂ with d–d transition, oxygen vacancies and Ti³⁺ centers: Synthesis, characterisation, UV-vis photocatalytic and mechanistic studies. *Ind. Eng. Chem. Res.*, 55(23), 6619–6633. <https://doi.org/10.1021/acs.iecr.6b01104>
20. Santara, B. et al. (2013). Evidence of oxygen vacancy induced room temperature ferromagnetism in solvothermally synthesised undoped TiO₂ nanoribbons. *Nanoscale*, 5(12), 5476. <https://doi.org/10.1039/c3nr00799e>
21. Ghorai, A. et al. (2016). Highly luminescent WS₂ quantum dots/ZnO heterojunctions for light emitting devices. *ACS Appl. Mater. Interfaces*, 9(1), 558–565. <https://doi.org/10.1021/acsami.6b12859>
22. Vanheusden, K. et al. (1996). Mechanisms behind green photoluminescence in ZnO phosphor powders. *J. Appl. Phys.*, 79(10), 7983–7990. <https://doi.org/10.1063/1.362349>
23. Pal, M. et al. (2012). Effects of crystallisation and dopant concentration on the emission behavior of TiO₂: Eu nanophosphors. *Nanoscale Res. Lett.*, 7(1), 1. <https://doi.org/10.1186/1556-276x-7-1>
24. Ahn, C. H. et al. (2009). A comparative analysis of deep level emission in ZnO layers deposited by various methods. *J. Appl. Phys.*, 105(1), 013502. <https://doi.org/10.1063/1.3054175>
25. Cao, B., Cai, W. & Zeng, H. (2006). Temperature-dependent shifts of three emission bands for ZnO nanoneedle arrays. *Appl. Phys. Lett.*, 88(16), 161101. <https://doi.org/10.1063/1.2195694>

26. Nasseh, N. et al. (2020). Enhanced photocatalytic degradation of tetracycline from aqueous solution by a novel magnetically separable FeNi₃/SiO₂/ZnO nanocomposite under simulated sunlight: Efficiency, stability and kinetic studies. *J. Mol. Liq.*, 301, 112434. <https://doi.org/10.1016/j.molliq.2019.112434>
27. Zhang, H. et al. (2018). Enhanced photocatalytic degradation of ciprofloxacin using novel C-dot@Nitrogen Deficient g-C₃N₄: Synergistic effect of nitrogen defects and C-dots. *Appl. Surf. Sci.*, 465, 450–458. <https://doi.org/10.1016/j.apsusc.2018.09.183>
28. Shi, W., Guo, F. & Yuan, S. (2017). *In situ* synthesis of Z-scheme Ag₃PO₄/CuBi₂O₄ photocatalysts and enhanced photocatalytic performance for the degradation of tetracycline under visible light irradiation. *Appl. Catal. B.*, 209, 720–728. <https://doi.org/10.1016/j.apcatb.2017.03.048>
29. Yan, Q. et al. (2016). Efficient photocatalytic degradation of tetracycline hydrochloride by Ag₃PO₄ under visible-light irradiation. *Environ. Sci. Pollut. Res.*, 23(14), 14422–14430. <https://doi.org/10.1007/s11356-016-6588-2>